Research Square

Preprints are preliminary reports that have not undergone peer review.
They should not be considered conclusive, used to inform clinical practice,
or referenced by the media as validated information.

A Physics-Guided Transfer Learning Framework for Cloud, Dust and Clear-Sky Detection over Bright Surfaces in Passive Satellite Remote Sensing

Sichen Wang
Lanzhou University
Tianhe Wang
wangth@lzu.edu.cn

Lanzhou University
Yingzi Jiao
Lanzhou University
Wenge Han
Lanzhou University
Jingtao Li
Lanzhou University
Xi Mu
University of Science and Technology of China
Jingyi Tang
Lanzhou University
Fan Yang
China Meteorological Administration
Chenglong Zhou
China Meteorological Administration
Bakhriddin E. Nishonov
The Hydrometeorological Research Institute
Mansur O. Amonov
The Tashkent Institute of Irrigation & Agricultural Mechanization Engineers, National Research University

---

Article

Keywords: Cloud detection, Dust detection, Satellite remote sensing, Radiative transfer simulation, Transfer learning, Stochastic differential equation network

Posted Date: September 4th, 2026

DOI: https://doi.org/10.21203/rs.3.rs-10778593/v1

License: This work is licensed under a Creative Commons Attribution 4.0 International License.
Read Full License

Additional Declarations: No competing interests reported.

A Physics-Guided Transfer Learning Framework for Cloud, Dust and Clear-Sky Detection over Bright Surfaces in Passive Satellite Remote Sensing

Sichen Wang[a], Tianhe Wang[a,*], Yingzi Jiao[a], Wenge Han[a], Jingtao Li[a], Xi Mu[b], Jingyi Tang[a], Fan Yang[c], Chenglong Zhou[c], Bakhriddin E. Nishonov[d, e], Mansur O. Amonov[f]

a. The Key Laboratory for Semi-Arid Climate Change of the Ministry of Education, College of Atmospheric Sciences, Lanzhou University, Lanzhou 730000, China

b. University of Science and Technology of China, Hefei 230026, China

c. The Institute of Desert Meteorology, China Meteorological Administration, Urumqi 830002, China

d. The Hydrometeorological Research Institute, Tashkent 100052, Uzbekistan

e. Central Asian University of Environmental and Climate Change Studies (Green University), Tashkent 100052, Uzbekistan

f. The Tashkent Institute of Irrigation & Agricultural Mechanization Engineers, National Research University, Tashkent 100000, Uzbekistan

** Corresponding author. E-mail address: wangth@lzu.edu.cn*

ABSTRACT

Accurate discrimination among clouds, dust aerosols, and bright surfaces remains challenging because these targets exhibit substantial spectral overlap. Fixed-threshold algorithms often lack regional transferability, whereas data-driven models are constrained by sparse and potentially biased reference labels. This study presents a physics-guided transfer-learning framework based on a stochastic differential equation network (SDE-Net) for joint cloud and dust aerosol identification from MODIS multispectral observations. Radiative transfer simulations spanning a broad range of atmospheric, surface, and viewing conditions were used for model pretraining, and collocated MODIS-CALIPSO observations were used for regional fine-tuning. The proposed method achieved overall accuracies of 93.81% and 85.68% for daytime and nighttime classification, respectively. For dust aerosol identification, the overall accuracy was 91.96%, and the daytime and nighttime F1 scores were 87.80% and 77.04%, respectively, exceeding those of the evaluated benchmark methods by 3.22% to 27.01%. Cloud recall reached 95.09% during daytime and 92.61% at night. Case studies showed that the retrieved spatial patterns were more consistent with MODIS imagery and CALIPSO vertical feature observations than the comparison products. The stochastic formulation further enabled uncertainty quantification. Mean epistemic uncertainty remained low at 1.71% during daytime and 5.69% at night, whereas mean aleatoric uncertainty increased from 14.96% to 31.40%. The proposed framework provides an effective approach for cloud-dust discrimination over bright surfaces and supports subsequent environmental and climate analyses.

Keywords: Cloud detection; Dust detection; Satellite remote sensing; Radiative transfer simulation; Transfer learning; Stochastic differential equation network

1. Introduction

Reliable cloud and dust masks are essential for many downstream satellite products. This task is particularly challenging in the arid regions of Central Asia, where dust sources coexist with seasonal snow, complex terrain, and frequent cloud systems. Passive satellite radiances measured at the top of the atmosphere (TOA) contain contributions from both the atmosphere and the underlying surface. Over bright surfaces, the surface contribution can dominate the observed signal and reduce the contrast of atmospheric features (Jiao et al., 2026, Kokhanovsky et al., 2007; Nakajima et al., 2011; Hsu et al., 2013). Classification errors under these conditions propagate into higher-level satellite products and can bias estimates of cloud-aerosol interactions and the regional energy balance (Arola et al., 2022; Jia et al., 2021; Zhang et al., 2020).

Clouds and dust aerosols differ in particle size, composition, and optical behavior. The imaginary refractive index of dust is approximately 0.0001 – 0.008, and the single-scattering albedo generally exceeds 0.8 (Di Biagio et al., 2019; Kim et al., 2011; Wang et al., 2024). Cloud particles are larger and nearly nonabsorbing at visible wavelengths, resulting in strong multiple scattering and high reflectance (Platnick et al., 2017; King et al., 1997; Kindel et al., 2011). These differences are also evident in the thermal infrared. Cloud-top brightness temperatures are often lower than surface temperatures, whereas mineral dust exhibits a characteristic but variable silicate absorption signature at approximately 8 to 12 μm (Ackerman et al., 1998; Li et al., 2003). These spectral contrasts provide the physical basis for many threshold-based cloud and dust detection methods (Derrien et al., 1993; Foga et al., 2017; Gupta and Panchal, 2015; Le Borgne et al., 2013; Mahajan and Fataniya, 2020; Park et al., 2014; Platnick et al., 2003).

Commonly used physical threshold methods include the normalized difference dust index (NDDI), brightness temperature differences (BTDs), and combinations of multispectral thresholds (Ackerman, 1989, 1997; Wald et al., 1998; Roskovensky and Liou, 2003, 2005; Qu et al., 2006). However, surface reflectance and emissivity, atmospheric loading, and observation geometry all modify the satellite signal. Consequently, thresholds calibrated for one region or atmospheric state may perform poorly elsewhere. For example, NDDI thresholds of 0.26 and 0.18 have been reported for dust detection in Inner Mongolia and Iraq, respectively (Li and Song, 2009; Albarakat and Lakshmi, 2019). Threshold-based methods are therefore physically interpretable but difficult to generalize across heterogeneous surfaces and observing conditions.

Machine-learning methods provide flexible solutions for complex pattern-recognition tasks (Gui et al., 2024; Kussul et al., 2017; Zhang et al., 2016; Zhu et al., 2017). Deep neural networks (Hou et al., 2020), support vector machines (Shi et al., 2020), random forests (Souri and Vajedian, 2015), generative adversarial networks (Wu et al., 2019; Xu et al., 2022), and transformer models (Zhang et al., 2022; Zhen et al., 2024) have been applied to cloud and dust aerosol identification and often outperform spectral-index tests. These methods can learn nonlinear interactions among the atmosphere, surface, and viewing geometry. Nevertheless, greater model capacity does not by itself ensure reliable generalization because the learned decision boundary ultimately depends on the quality and representativeness of the training data.

Reliable reference labels remain a major constraint on machine-learning approaches to cloud-dust discrimination (Aybar et al., 2024; Foga et al., 2017; Wang et al., 2024). In computer vision, benchmark datasets are commonly established through expert annotation (Rasmussen et al., 2022). For satellite observations, however, clouds, dust, snow, and bright soil can have similar visual and spectral characteristics, making expert interpretation uncertain even when HSV composites or

thermal-infrared RGB imagery are available. At night, the absence of reflected solar measurements further limits visual verification (Boloorani et al., 2023; Fuell et al., 2016). Secondary satellite products, such as aerosol optical depth or aerosol index products, can assist label generation, but this strategy can propagate errors from the cloud and aerosol screening procedures used to generate those products (Rivas-Perea et al., 2013; Shi et al., 2019; Souri and Vajedian, 2015).

Spaceborne lidar provides a valuable alternative because it resolves vertical atmospheric structure and is less sensitive to surface radiance. The Cloud – Aerosol Lidar and Infrared Pathfinder Satellite Observation (CALIPSO) mission combines backscatter and depolarization measurements to distinguish clouds from dust and provides reference classifications during both daytime and nighttime (Chen et al., 2012; Hagihara et al., 2010). CALIPSO labels have been used to train dust classifiers for the Visible Infrared Imaging Radiometer Suite (Lee et al., 2021) and Himawari-8 (Jin et al., 2023). However, spaceborne lidar provides only narrow along-track sampling. Consequently, collocated datasets may underrepresent rare surface types, viewing geometries, and atmospheric states.

Radiative transfer models have been used to generate large simulated datasets that improve the physical coverage of model training. These simulations can reproduce satellite TOA observations over a wide range of surface and atmospheric conditions, and simulation-based classifiers have shown promising performance for cloud and haze detection from MODIS observations (Jiao et al., 2023). Nevertheless, simulated radiances remain approximations of actual measurements. Aerosol mixtures, cloud microphysics, three-dimensional radiative effects, and surface anisotropy cannot be represented completely. A classifier trained exclusively on simulations may therefore perform poorly on satellite observations because of residual differences between the simulated and observed domains.

Transfer learning provides a direct means of combining radiative transfer simulations with lidar measurements. A model can first learn general spectral relationships from simulations and then adapt these relationships to real measurements using a smaller observational dataset (Weiss et al., 2016; Torrey and Shavlik, 2010; Zhuang et al., 2020; Pan and Yang, 2009). Similar strategies have improved satellite retrievals when only limited ground-based observations were available for training (Fu et al., 2024; Tang et al., 2025). However, the potential of this approach for joint cloud and dust aerosol detection across the full diurnal cycle has received limited attention.

This study proposes a transfer-learning framework that combines the broad physical coverage of radiative transfer simulations with the observational constraints provided by CALIPSO to identify clouds and dust aerosols over bright surfaces. Solar-reflective and thermal-infrared MODIS observations were simulated for clouds and dust under diverse surface types and viewing geometries. These simulations were used to pretrain a classifier based on SDE-Net, which was subsequently fine-tuned using CALIPSO vertical feature classifications collocated with MODIS. The continuous stochastic formulation of SDE-Net further enabled quantitative assessment of predictive uncertainty.

2. Study area and data

2.1. Study area

The study domain covers the major arid and semiarid regions of Central and East Asia, extending approximately from 60°E to 110°E and from 25°N to 50°N (Fig. 1). It includes several major dust source regions, including the Karakum, Moiynkum, Taklimakan, and Qaidam deserts, where extensive bare soil and sparse vegetation produce high surface albedo. The Tibetan Plateau,

known as the "Asian Water Tower," is also included and is characterized by complex terrain, extensive seasonal snow cover, and frequent clouds. The coexistence of active dust sources, bright surfaces, and variable atmospheric conditions provides a challenging environment for evaluating cloud and dust aerosol detection.

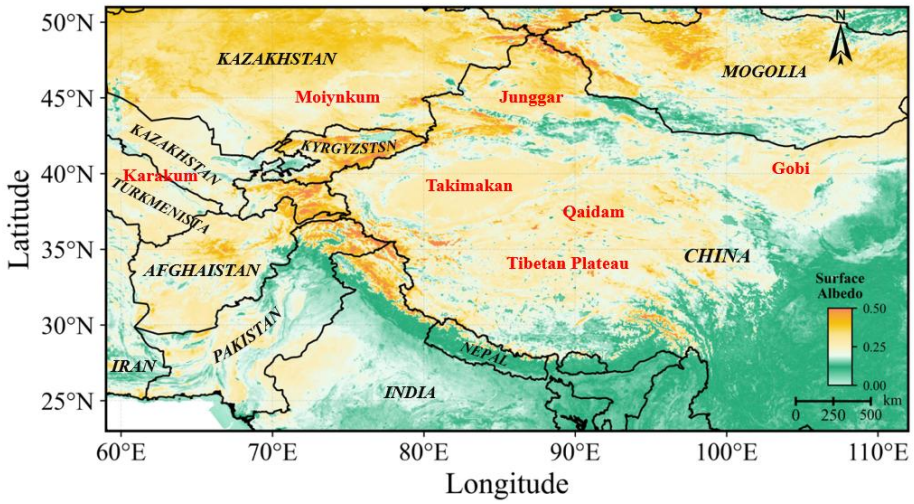


Fig. 1. Study area. Red labels indicate important geographical regions, including deserts and plateaus. The background shows the 2017 annual mean surface albedo derived from the MODIS MCD43C3 product.

2.2. Data

The datasets used in this study comprise 2017 Aqua MODIS products, CALIPSO lidar products, and ERA5 reanalysis. The MODIS products include MYD021KM, MYD03, MCD12Q1, and MYD35, which provide radiometric measurements, geolocation and viewing geometry, land-cover classification, and cloud-mask information, respectively. The CALIPSO vertical feature mask (VFM) product provides cloud and aerosol classifications, whereas ERA5 skin temperature characterizes surface thermal conditions. Table 1 summarizes these datasets.

Table 1. Data used in this study

Name	Description	Spatial/temporal resolution	Source
MCD12Q1	MODIS land-cover product (IGBP classification)	500 m/yearly	NASA
MYD021KM	Aqua MODIS Level-1B product	1 km/daily	
MYD03	Aqua MODIS geolocation product		
MYD35	Aqua MODIS cloud-mask product		
CALIPSO VFM	CALIPSO Level-2 333-m feature-layer product	333 m/daily	
ERA5 skin temperature	Temperature of the Earth's surface	0.25° /hourly	ECMWF

2.2.1. MODIS products

The Aqua MODIS instrument was launched on 4 May 2002 as part of the NASA Afternoon Constellation and provides continuous multispectral observations for Earth observation. The Aqua MODIS Level-1B product (MYD021KM) contains calibrated radiances for 36 spectral bands

spanning the visible to thermal-infrared regions. MODIS reflectances and brightness temperatures used in this study were derived from MYD021KM.

The MYD03 geolocation product provides pixel-level geographic and observation-geometry information for Aqua MODIS, including latitude, longitude, solar zenith and azimuth angles, and sensor zenith and azimuth angles. These variables were used to geolocate MYD021KM pixels and to support spatial collocation with the other datasets.

The MCD12Q1 land-cover product provides annual global land-cover classifications at 500 m resolution based on combined Terra and Aqua MODIS observations. The International Geosphere–Biosphere Programme classification was used in this study to describe surface types.

The MODIS cloud-mask product (MYD35) was used to evaluate the proposed model. The MYD35 algorithm estimates cloud and clear-sky confidence through a series of visible and infrared threshold tests combined with spectral and spatial consistency checks. As a widely used operational cloud-screening product, MYD35 provides an independent benchmark for the proposed identification method.

2.2.2. Lidar and reanalysis data

The CALIPSO VFM product was used for model fine-tuning and validation. Launched in April 2006, CALIPSO carries the Cloud–Aerosol Lidar with Orthogonal Polarization, which measures vertically resolved backscatter and polarization signals from clouds and aerosols. The VFM product classifies atmospheric features along the CALIPSO ground track and therefore provides a physically meaningful reference for distinguishing clouds from dust aerosols. Reference labels were generated by decoding the CALIPSO VFM flags according to the following criteria.

a. Spatial collocation: MODIS pixels were matched to CALIPSO VFM observations using a nearest-neighbor search within a 500-m radius. Only VFM observations with a quality-assurance value of 3 and a cloud-aerosol discrimination score of at least 75 were retained.
b. Cloud label: A profile was labeled as cloud when it contained only cloud features or when the uppermost atmospheric layer was identified as an opaque cloud.
c. Dust label: A profile was labeled as dust when it contained only dust or polluted-dust features.
d. Clear-sky label: A profile was labeled as clear sky when it contained only clear air or features that were classified as neither cloud nor dust.
e. Consistency check: When multiple CALIPSO VFM observations were matched to one MODIS pixel, a label was assigned only if all retained observations indicated the same class. Samples with mixed or inconsistent CALIPSO labels were excluded from training and evaluation.

ERA5 skin temperature data were obtained from the European Centre for Medium-Range Weather Forecasts and used as auxiliary surface thermal information. Skin temperature represents the temperature of the uppermost surface layer and is closely related to surface radiation and heat exchange. It was used to characterize the surface thermal state corresponding to each satellite observation.

3. Method

Fig. 2 summarizes the proposed workflow. Multiscenario MODIS observations of clouds and aerosols were generated with a radiative transfer model and used as source-domain data for pretraining. Collocated MODIS-CALIPSO samples were then used as target-domain data to fine-tune the pretrained model, thereby adapting the simulation-informed representation to real satellite observations.

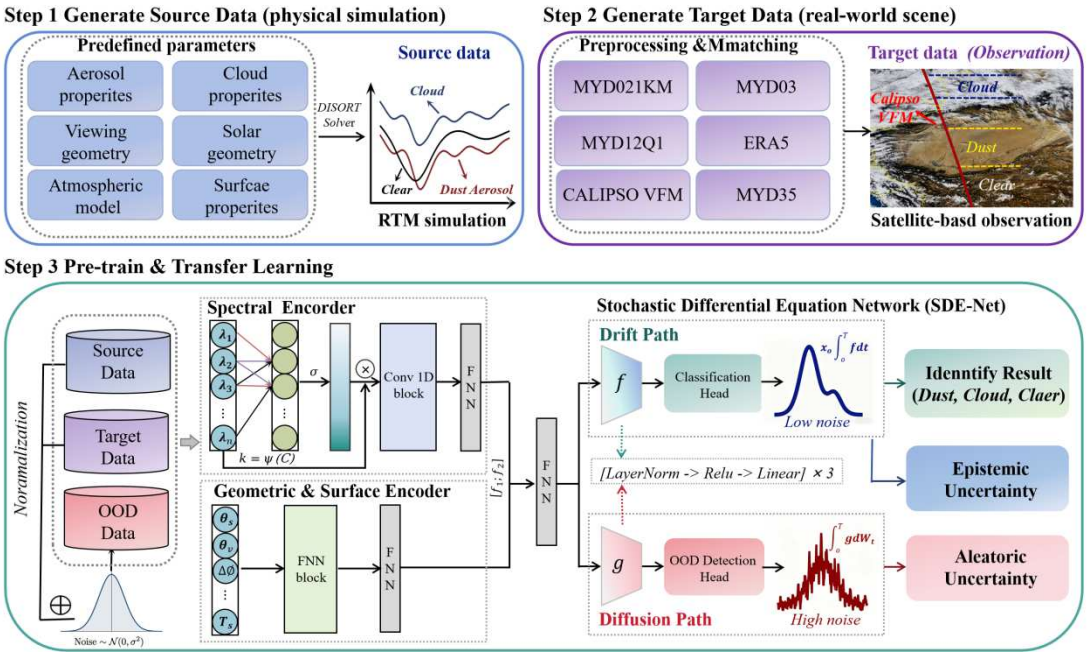


Fig. 2. Workflow of the proposed method. Radiative transfer simulations generate source-domain spectra using dust aerosol, cloud, atmospheric, surface, and observation-geometry parameters (Step 1). MODIS, CALIPSO, and ERA5 products are collocated to construct the target-domain dataset (Step 2). SDE-Net is pretrained on the simulated data and subsequently fine-tuned using the target-domain dataset to classify clear sky, dust, and cloud and estimate uncertainties (Step 3).

3.1. Radiative transfer simulation

The libRadtran package was used to calculate MODIS TOA reflectances and brightness temperatures for the channels selected as model inputs. libRadtran is an open-source radiative transfer package developed for simulating solar and thermal radiation in the atmosphere (Emde et al., 2016; http://www.libradtran.org). Table 2 summarizes the atmospheric conditions, surface parameters, and associated optical properties used in the simulations.

Table 2. Types of atmospheric and surface parameters selected for simulation

Configurations	Selection	Source	Optical properties
Atmospheric trace gases	U.S. Standard atmosphere constituent profiles	Anderson et al., 1986	Extinction coefficient
Water clouds	Mie – Debye theory	Mishchenko et al., 2002	Single scattering albedo
Ice clouds	General habit mixture model	Baum et al., 2011	Scattering phase function
Molecular scattering optical depths	Rayleigh scattering cross section	Stamnes et al., 2018	Reflectance function
Surface properties	IGBP library	Loveland and Belward, 1997	

The U.S. Standard Atmosphere (Anderson et al., 1986) was used to construct the atmospheric profiles. It specifies pressure, temperature, air density, and the concentrations of H_2O, NO_2, O_2, CO_2, O_3, and CH_4. Rayleigh-scattering cross sections were calculated from the pressure profiles in the atmospheric parameter files. Mie calculations were used for liquid-cloud particles, with liquid water

content and effective radius converted to optical properties using precomputed lookup tables containing the complete scattering phase matrices. These lookup tables are available from the libRadtran website.

Table 3. Configuration of the radiative transfer simulation model

Parameter	Range	Description
SZA	0–80°	Solar zenith angle
VZA	0–80°	Viewing zenith angle
RAA	0–180°	Relative azimuth angle
AOD	0 – 5	Aerosol optical depth
Aerosol type	antarctic, continental average/polluted, desert, urban	Aerosol optical properties specified in the OPAC library
COD_w	0–15	Water cloud optical depth
COD_i	0–15	Ice cloud optical depth
Surface type	1–16	IGBP-defined land cover types
Surface temperature	250–305 K	Used to calculate the thermal infrared emission from the surface

The Baum ice-cloud parameterization was used to convert microphysical properties, including effective radius, into extinction coefficients, asymmetry factors, and single-scattering albedos. Aerosol optical properties were obtained from the optical properties of aerosols and clouds (OPAC) database by combining particle-size distributions with refractive indices. Surface anisotropy was represented using the Rahman-Pinty-Verstraete bidirectional reflectance distribution function available in libRadtran. Surface classes were specified using the embedded IGBP database derived from the NASA Clouds and the Earth's Radiant Energy System surface-property dataset. Sixteen IGBP surface classes (classes 1 to 16) were included in the simulations. Table 3 lists the complete simulation configuration, and Fig. S1 and S2 show representative TOA reflectance and brightness temperature spectra, respectively.

3.2. Deep learning model

3.2.1. Feature encoding

The inputs were divided into spectral variables (reflectances and brightness temperatures) and auxiliary variables (observation geometry and surface properties), which were processed by two independent encoders. A one-dimensional convolutional neural network (1D-CNN) was used to represent correlations among spectral bands. For the spectral input $X_{spec} \in R^s$, where S denotes the number of spectral bands, a channel-attention module was used to assign a weight to each band:

$$\omega = \sigma\left(Conv1D_k(s)\right) \tag{1}$$

where σ denotes the sigmoid function, and $Conv1D_k$ represents a one-dimensional convolution with kernel size k. Specifically, the attention weight for channel i, denoted by ω_i was calculated from the interaction between s_i and its k neighboring channels:

$$\omega_i = \sigma\left(\sum_{j=1}^{k} w^j z_i^j\right), \quad z_i^j \in \Omega_i^k \tag{2}$$

where Ω_i^k denotes the set of k channels adjacent to z_i. The kernel size k determines the extent of local cross-channel interaction and was adaptively calculated from the spectral dimension C:

$$k = \psi(S) = \left| \frac{log_2(C)}{\gamma} + \frac{b}{\gamma} \right|_{odd} \quad (3)$$

where $|\cdot|_{odd}$ denotes the nearest odd integer, and γ and b are hyperparameters.

The channel-attention weights were applied to the spectral features by channel-wise multiplication:

$$\widetilde{X}_{spec} = \omega \odot X_{spec} \quad (4)$$

where $\odot$ denotes element-wise multiplication with broadcasting along the spectral dimension.

The reweighted spectral features $\widetilde{\mathrm{X}}_{\mathrm{spec}}$ were then processed by three stacked 1D convolutional blocks, each comprising a convolutional layer, layer normalization, and a rectified linear unit activation. A fully connected network subsequently produced the spectral representation $\mathrm{h}_{\mathrm{spec}}$.

Land-cover classes were one-hot encoded and concatenated with observation geometry and skin temperature to form the auxiliary input vector. A three-layer fully connected network encoded this vector as $\mathrm{h}_{\mathrm{geo}}$. The spectral and auxiliary representations were concatenated and mapped through a fully connected layer to the initial state of the stochastic dynamical system:

$$x_0 = W\left[\mathrm{h}_{spec}\,;\,\mathrm{h}_{geo}\right] + b \quad (6)$$

3.2.2. Stochastic differential equation network

Following the stochastic differential equation network framework of Kong et al. (2020), the hidden representation was modeled as a continuous-time stochastic process. The initial state x_0 was evolved over the time interval $[0,\ \mathrm{T}]$ according to

$$dx_t = f(x_t, t; \theta_f)dt + g(x_0; \theta_g)dW_t \quad (7)$$

where the drift function $f(\cdot;\theta_f)$ takes a d-dimensional state vector and time t within the interval from 0 to T. The diffusion function $g(x_0;\theta_g)$ takes the initial state x_0 as input and returns a $d \times m$ matrix that controls the magnitude of the m-dimensional Brownian motion W_t.

The SDE was solved using the Euler–Maruyama method on the fixed time grid $t_0<t_1<\ldots<t_k=T$, with K=10. The discrete update was

$$x_{t_{k+1}} = x_{t_k} + f(x_{t_k}, t_k; \theta_f)\Delta t + g(x_0; \theta_g)\sqrt{\Delta t}Z_k,\ \Delta t = T/k \quad (8)$$

where $Z_k \sim N(0, 1)$ is a standard Gaussian random variable. The final state x_t was passed through a linear classifier and softmax function to obtain the probabilities of clear sky, cloud, and dust aerosol.

The stochastic formulation enables separate characterization of epistemic and aleatoric uncertainty. Epistemic uncertainty reflects limitations in model knowledge caused, for example, by insufficient or unrepresentative training samples. Aleatoric uncertainty reflects ambiguity in the observations or class definitions, including sensor noise, mixed pixels, and interference from bright surfaces. This component represents classification ambiguity that cannot be fully eliminated through model training.

For each input, 20 stochastic forward realizations of the trained SDE-Net were generated. Aleatoric uncertainty U was calculated as the normalized expected predictive entropy of the three-class output:

$$U = \frac{E_{p(x_T|x_0,\,\theta_f,g)}\left[\mathcal{H}[p(y|x_T)]\right]}{logN} \times 100\% \quad (9)$$

where y indexes the predicted classes (clear sky = 0, cloud = 1, and dust aerosol = 2), and N is the number of classes. The entropy was normalized by the maximum value $logN$ and expressed on a scale from 0% to 100%.

Epistemic uncertainty is commonly represented by the variance of the terminal state $Var(x_T)$. Because variance is less intuitive as a percentage measure, predictive entropy for out-of-distribution

samples along the diffusion trajectory was used as a surrogate measure of epistemic uncertainty, with N set to 2 for this calculation.

3.3. Model evaluation

The collocated MODIS-CALIPSO samples were divided into training, validation, and test subsets at a ratio of 2:1:1, corresponding to 50%, 25%, and 25% of the samples, respectively. The proposed model and all benchmark methods were evaluated using the same data split. Separate models were trained and evaluated for daytime and nighttime because the available input variables differed. Performance was assessed using overall accuracy; class-specific precision, recall, and F1 score; macro- and weighted-F1 scores; the area under the receiver operating characteristic curve (ROC-AUC); and confusion matrices. For comparison with MYD35, cloud recall and cloud F1 score were calculated under two definitions of cloudy pixels based on the MYD35 confidence levels. Cloud-to-clear, clear-to-cloud, and dust-to-cloud error rates were also calculated. Supplementary Methods S1 and S2 provide the corresponding equations.

3.4. Feature importance analysis

Shapley additive explanations (SHAP) were used to quantify the contributions of variables from the two input branches. The spectral branch comprised MODIS reflectances and brightness temperatures, whereas the auxiliary branch comprised observation geometry, land-cover class, and ERA5 skin temperature. Although the branches were encoded independently and subsequently fused, SHAP attributed the final output to the original variables, allowing all contributions to be compared on a common scale. The SHAP value of feature i was defined as

$$\phi_i = \sum_{S \subseteq F_{-i}} \frac{|S|!\,(|F| - |S| - 1)!}{|F|!} [f(S + i) - f(S)] \tag{10}$$

where F is the complete input feature set; F_{-i} is the set excluding feature i; S is a subset of F_{-i}; $S + i$ is the subset after adding feature i to S; and $f(\cdot)$ is the model output. Global feature importance was calculated as the mean absolute SHAP value across the test samples; a larger value indicates a greater average contribution to classification.

4. Results and discussion

4.1. Overall performance evaluation

Fig. 3 summarizes performance on the independent test subset. During daytime, the overall accuracy was 0.94, and recall values were 94.94% for clear sky, 95.09% for cloud, and 84.98% for dust aerosol. At night, the overall accuracy decreased to 0.86. Cloud recall remained high at 92.61%, whereas dust and clear-sky recall decreased to 81.32% and 81.78%, respectively. The dominant daytime confusion occurred between clear sky and dust aerosol, indicating that dust identification was more sensitive than cloud identification to interference from the underlying surface.

The ROC curves in Fig. 3b further demonstrate the discriminative capability of the model. Daytime AUC values were 0.984, 0.993, and 0.987 for clear sky, cloud, and dust aerosol, respectively; the corresponding nighttime values were 0.943, 0.988, and 0.953. Although all nighttime AUC values were lower than their daytime counterparts, they remained high, indicating that the model retained strong probabilistic discrimination when solar-reflective information was unavailable.

The summary metrics in Fig. 3c show that the daytime model achieved an accuracy of 0.94, a macro-F1 score of 0.92, and a weighted-F1 score of 0.94; the corresponding nighttime values were 0.86, 0.85, and 0.86. Cloud was the most stable class across the diurnal cycle, with the F1 score decreasing only from 0.96 during daytime to 0.94 at night. By contrast, the dust F1 score decreased from 0.88 to 0.77, confirming the greater difficulty of nighttime dust identification. The land-cover-stratified results in Fig. 3d further indicate that daytime performance remained high over vegetated, urban, bare, and snow/ice surfaces, whereas nighttime performance showed a stronger surface dependence, particularly for clear sky and dust aerosol over bare surfaces.

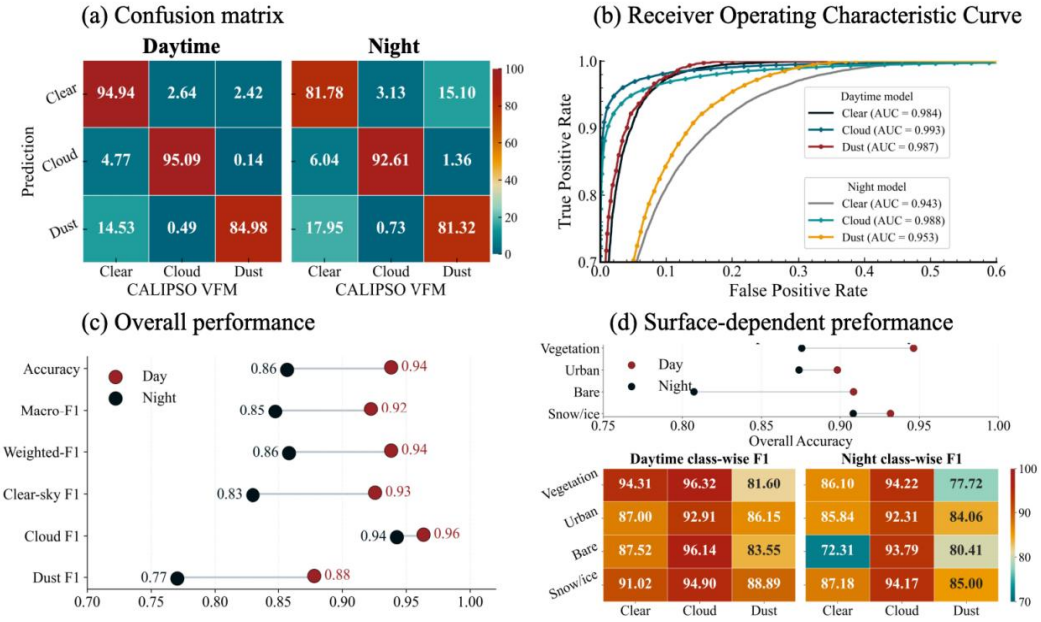


Fig. 3. Test performance of the proposed model. (a) Confusion matrices, (b) ROC curves, (c) overall and class-wise metrics, and (d) surface-dependent performance.

4.2. Identification case studies

Representative cases were selected to examine the spatial behavior of the model (Fig. 4). Each classification map was compared with the corresponding MODIS imagery, MYD35 cloud mask, and CALIPSO VFM profile. Fig. 4a shows a dust storm over the Taklimakan Desert. In region A, the MODIS RGB composite contains a distinct yellow-brown dust signature. MYD35 classifies much of this region as cloud, whereas the proposed model retrieves a spatially continuous dust plume. Region B illustrates cloud detection over the snow-covered Tibetan Plateau. MYD35 identifies the bright surface as cloud, whereas the proposed model substantially reduces this false detection. The collocated CALIPSO VFM profile confirms the absence of a corresponding cloud layer in region B.

Fig. 4b presents nighttime cases, for which the 11-μm brightness temperature provides a visual reference because visible reflectances are unavailable. In region C, CALIPSO detected a distinct dust event over Central Asia. The proposed model retrieved a spatially consistent dust region and separated the plume from the background more clearly than MYD35. Regions D and E illustrate classification under more complex nighttime conditions. MYD35 omitted cloud features identified by CALIPSO in region D and classified a dust layer as cloud in region E, whereas the proposed model correctly identified the corresponding cloud and dust features.

Collectively, these cases demonstrate that the proposed method distinguishes dust aerosol, cloud, and clear-sky backgrounds under diverse illumination and surface conditions. The retrieved cloud and dust patterns are consistent with the corresponding MODIS imagery and CALIPSO observations in both daytime and nighttime scenes.

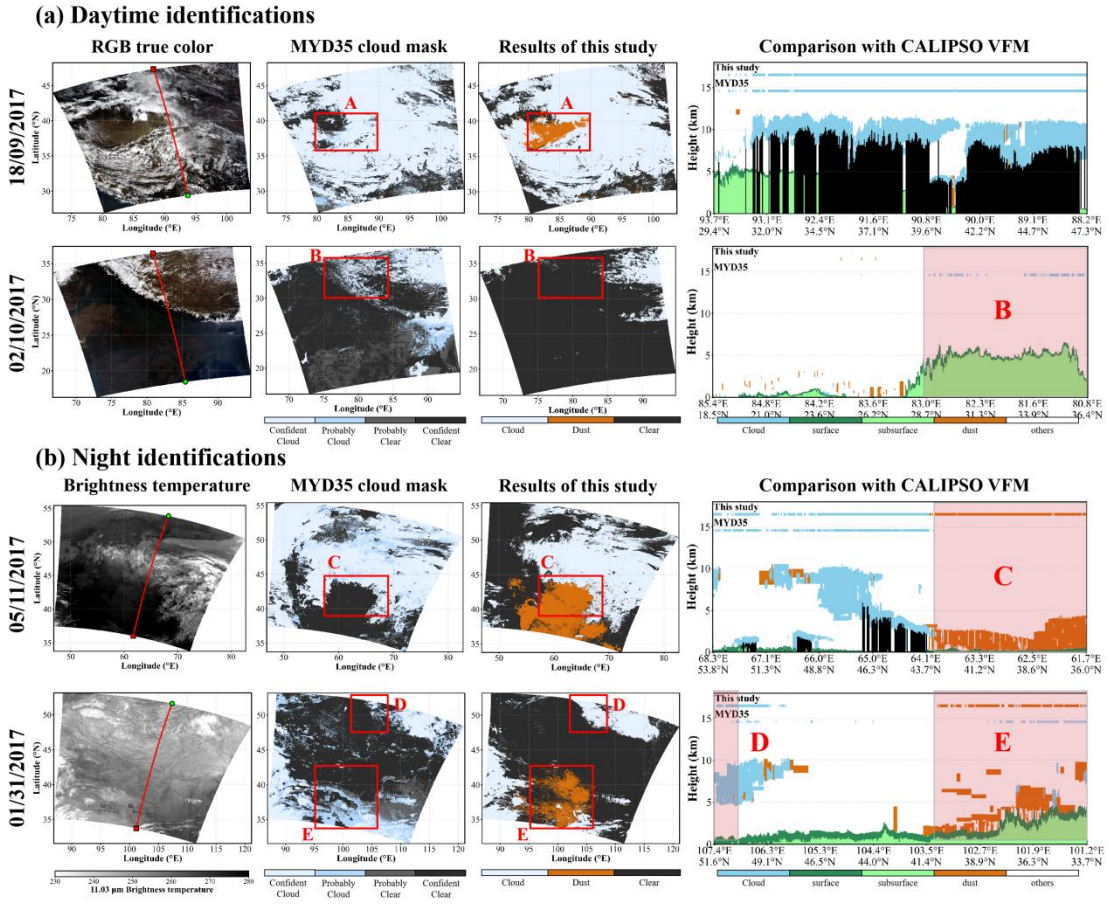


Fig. 4. Representative classification cases. (a) Daytime cases illustrating dust-cloud discrimination (region A) and cloud detection over snow-covered surfaces (region B). (b) Nighttime cases illustrating dust identification (region C), cloud-background discrimination (region D), and dust-cloud discrimination (region E) using thermal-infrared observations.

4.3 Uncertainty analysis

The uncertainty analysis separates ambiguity associated with the observations and reference data (aleatoric uncertainty) from limitations in model knowledge (epistemic uncertainty; Fig. 5a). Across the complete test subset, mean aleatoric uncertainty was substantially higher than mean epistemic uncertainty and increased from 14.96% during daytime to 31.40% at night. Mean epistemic uncertainty remained low, increasing from 1.71% to 5.69%. This combination indicates that the dominant limitation arises from the inherent difficulty of distinguishing clouds, dust aerosol, and bright surfaces from MODIS observations rather than from insufficient model knowledge.

Although epistemic uncertainty remained low overall, it was higher at night and reached its largest values over snow- and ice-covered surfaces, indicating less complete model knowledge for these relatively uncommon conditions. To investigate this pattern, encoded features from the radiative transfer simulations and MODIS-CALIPSO collocations were extracted from the final fine-tuned SDE-Net and jointly projected using one principal component analysis transformation (Fig. S3). The substantial class-conditional overlap between the two domains indicates that most

observations are represented within the simulation-informed feature space, consistent with the low overall epistemic uncertainty. Nevertheless, localized differences remain, and some observations occupy regions that are less adequately represented by the source-domain simulations.

The uncertainty maps for representative MODIS scenes support this interpretation (Fig. S4). Aleatoric uncertainty was spatially widespread and increased over heterogeneous cloud fields and transitions among atmospheric and surface classes, where spectral overlap and mixed pixels make the observations intrinsically ambiguous. Epistemic uncertainty was lower and more localized, with elevated values occurring primarily near class boundaries and under complex or sparsely represented conditions. Homogeneous and well-represented regions generally exhibited low epistemic uncertainty even when some observational ambiguity remained.

The perturbation experiment examined the response of the model to inputs that progressively departed from the training distribution (Fig. 5b). As perturbation magnitude increased, classification accuracy decreased monotonically from approximately 90% to 95% to 40% to 50%, whereas epistemic uncertainty increased from near 0% to almost 100%. At a perturbation level of approximately 5%, the daytime and nighttime models retained accuracies of approximately 80% and 70%, respectively. The concurrent decrease in accuracy and increase in epistemic uncertainty demonstrate that the model reports greater uncertainty for increasingly unfamiliar inputs.

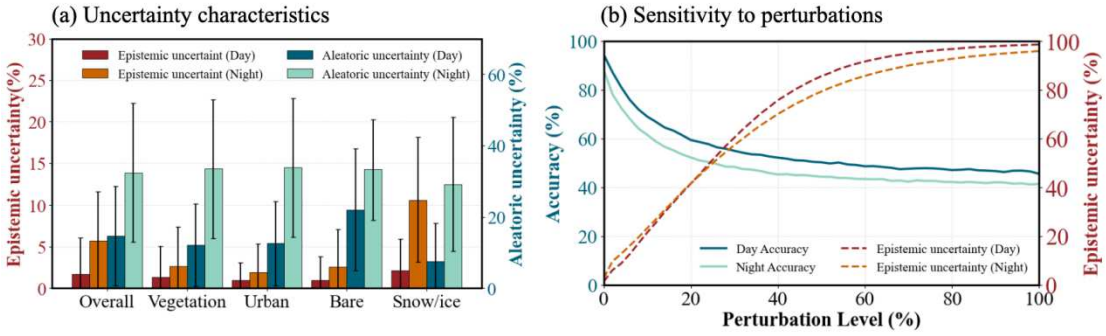


Fig. 5. Uncertainty characteristics of the proposed model. (a) Epistemic and aleatoric uncertainty for daytime and nighttime samples stratified by surface type. (b) Classification accuracy and epistemic uncertainty as functions of input perturbation magnitude.

4.4 Comparison with other methods

Because few existing methods identify clouds and dust aerosols simultaneously, dust and cloud performance was evaluated separately using binary metrics. Dust aerosol identification was compared with representative physical-threshold and machine-learning methods, whereas cloud identification was compared quantitatively with the operational MYD35 cloud-mask product.

4.4.1. Comparison with commonly used dust detection methods

Table 4 compares dust aerosol identification by the proposed model with representative threshold-based and machine-learning methods. The proposed model achieved the highest overall accuracy (91.96%), corresponding to relative improvements of 3.22% and 14.72% over the random forest and support vector machine, respectively. It also provided the most balanced performance across the diurnal cycle, with daytime and nighttime recall values of 84.98% and 81.32% and F1 scores of 87.80% and 77.04%, respectively.

The threshold-based methods showed clear limitations in balancing detection completeness against false alarms. For example, NDDI achieved a daytime recall of 93.68% but an F1 score of only 34.73%, indicating substantial overestimation. middle east dust index (MEDI) achieved a daytime recall of 78.87%, but its F1 score remained low at 43.12%. The BTD11–12 μm method supported nighttime detection, but its highest nighttime F1 score was 62.41%. These results demonstrate the sensitivity of fixed-threshold methods to the selected index, threshold, and illumination conditions. By contrast, the proposed model learned a multivariable decision boundary from spectral, thermal, geometric, and surface information and therefore provided more stable dust aerosol identification.

Table 4. Comparison between the proposed method and other dust identification algorithms

Method	Description	Threshold	Accuracy	Daytime		Night	
				Recall	F1	Recall	F1
$BTD_{11\text{-}12\ \mu m}$ (Ackerman, 1997)	Dust aerosol with $BT_{11} < BT_{12}$	-0.20	79.93	78.71	46.16	80.45	62.41
		-0.30	81.10	70.45	45.37	69.75	60.30
Normalized Difference Dust Index (NDDI) (Qu et al., 2006)	$NDDI = (\rho_{2.3} - \rho_{0.47}) / (\rho_{2.3} + \rho_{0.47})$	0.00	72.40	93.68	34.73	-	-
		0.20	83.46	67.07	38.87	-	-
Middle East Dust Index (MEDI) (Karimi et al., 2012)	$MEDI = (BTD_{11\text{-}8.5}) / (BTD_{12\text{-}8.5})$	0.85	85.33	30.44	24.54	-	-
		0.95	83.69	78.87	43.12	-	-
Normalized Dust Layer Index (NDLI) (Kazi et al., 2019)	Hybrid index method integrating visible, NIR and IR information	0.4	75.05	37.74	19.16	-	-
Random Forest (Souri and Vajedian, 2015)	Ensemble algorithm with multiple decision trees	-	89.09	67.41	74.34	71.52	69.29
Support Vector Machine (Shi et al., 2020)	Supervised algorithm with an optimal separating hyperplane	-	80.16	42.73	54.38	70.15	60.81
Transformer (Vaswani et al., 2017)	Self-attention-based neural network for modeling feature dependencies	-	88.42	65.96	74.61	71.08	68.47
This study	Transfer learning based on radiative transfer simulations	-	91.96	84.98	87.80	81.32	77.04

Two dust events over Mongolia and North China were selected for qualitative comparison; both contained substantial spatial mixing between cloud and dust. For the Mongolian event on 4 March 2016 (Fig. 6), the physical-threshold methods differed markedly in retrieved spatial coverage. BTD11-12 μm (Fig. 6b), Brightness temperature adjusted dust index (BADI) (Fig. 6d), and NDLI (Fig. 6f) identified broad dust regions, whereas MEDI (Fig. 6e) produced a more fragmented distribution and omitted part of the plume. The proposed model (Fig. 6g) produced a more coherent dust pattern that agreed more closely with the visible dust structure in the MODIS RGB composite (Fig. 6a).

Fig. 7 presents a strong dust storm over North China on 3 May 2017. The MODIS RGB composite shows a distinct brown dust signature and a clearly identifiable plume. With the exception of NDLI, which substantially overestimated the dust-affected area, the comparison methods and the proposed model generally captured the principal plume structure. Differences were more evident in cloud-dust transition zones and along plume margins, where the proposed method resolved finer dust structures within spectrally mixed pixels. The case therefore demonstrates an advantage in representing spatial detail under complex mixed conditions, even when the methods agree at the regional scale.

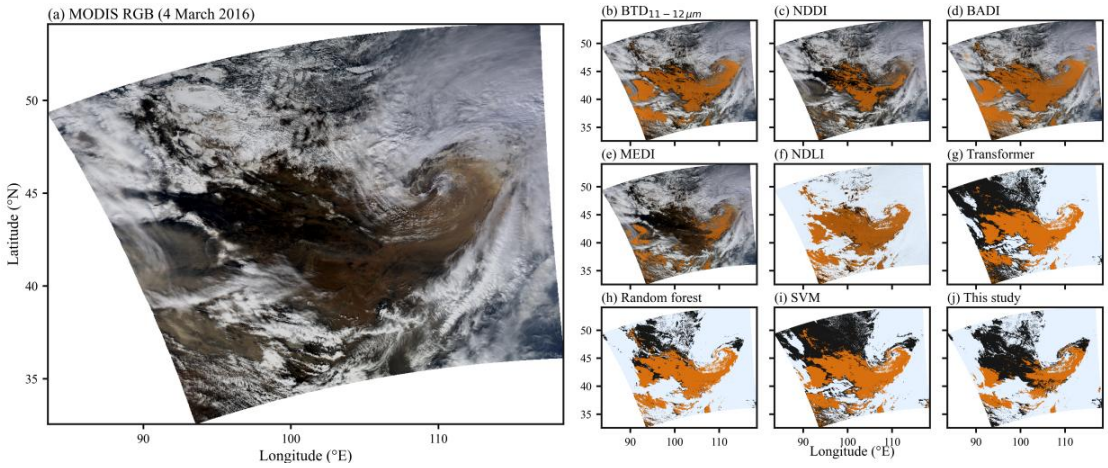


Fig. 6. Dust detection for the Mongolian event on 4 March 2016 using different methods. (a) MODIS true-color RGB composite. (b) Brightness temperature difference between 11 and 12 μm (BTD; threshold: −1 K). (c) Normalized difference dust index (NDDI; threshold: 0.26). (d) Brightness temperature adjusted dust index (BADI). (e) Middle east dust index (MEDI). (f) Normalized dust layer index (NDLI). (g) Transformer. (h) Random forest. (i) Support vector machine (SVM). (j) Classification produced by the proposed method.

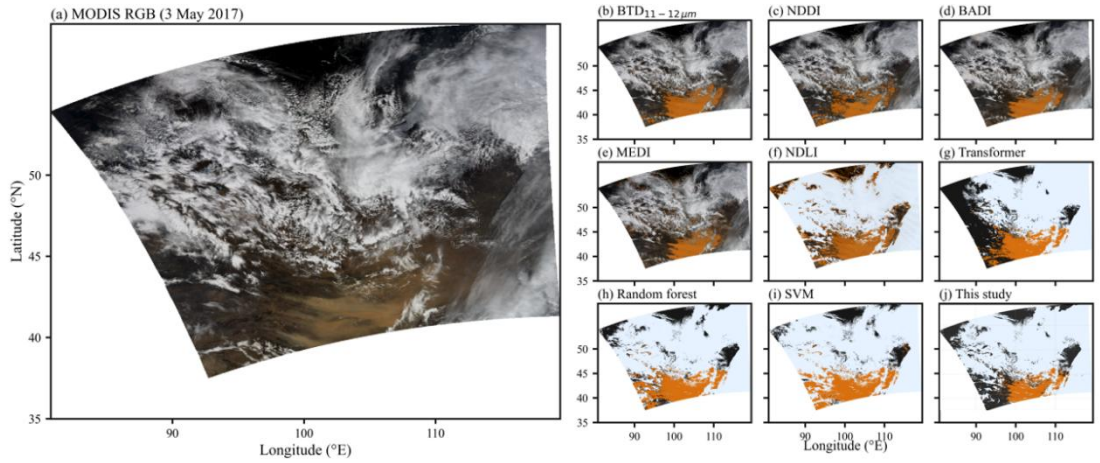


Fig. 7. As in Fig. 6, but for the dust event over North China on 3 May 2017.

4.4.2. Comparison with the operational MODIS cloud mask

The MODIS cloud-mask algorithm estimates the confidence that each pixel is clear or cloudy using a sequence of threshold tests and assigns one of four labels: 0, confident cloudy; 1, probably cloudy; 2, probably clear; and 3, confident clear. Two evaluation configurations were defined. In the strict configuration, only pixels labeled confident cloudy (class 0) or confident clear (class 3)

were retained. In the relaxed configuration, classes 0 and 1 were grouped as cloud, whereas classes 2 and 3 were grouped as clear sky.

Fig. 8 compares cloud identification by the proposed model with the two MYD35 configurations. During daytime, the proposed model achieved a cloud recall of 95.09% and a cloud F1 score of 96.35%, compared with F1 scores of 91.54% for the confident-only configuration and 87.43% for the relaxed configuration. These values correspond to relative improvements of 5.25% and 10.20%, respectively. Clear-to-cloud and dust-to-cloud errors were limited to 2.64% and 0.49%, indicating fewer false cloud detections over clear-sky and dust-affected pixels. At night, the proposed model maintained a cloud F1 score of 94.26%, compared with 89.12% and 80.90% for the two MYD35 configurations, corresponding to relative improvements of 5.77% and 16.51%. Cloud-to-clear and dust-to-cloud errors were 7.39% and 0.73%, respectively.

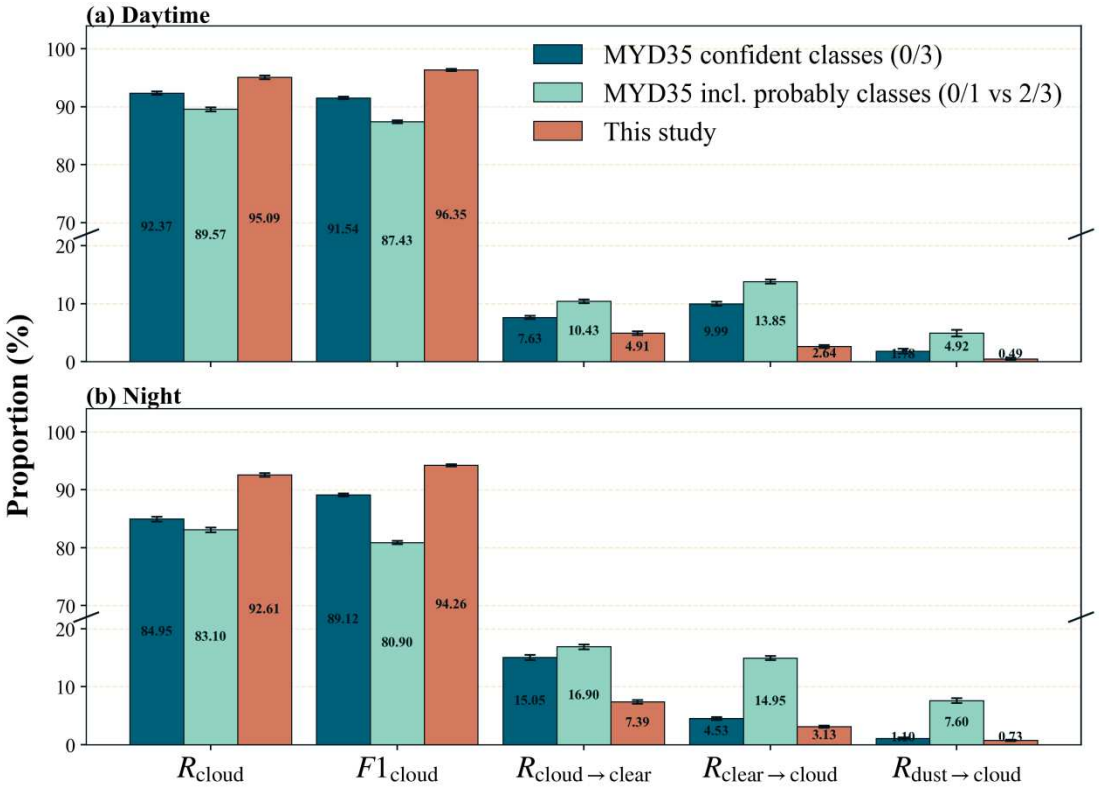


Fig. 8. Cloud detection performance of MYD35 and the proposed model during (a) daytime and (b) nighttime. Metrics include cloud recall, cloud F1 score, cloud omission, and false cloud detections for clear-sky and dust aerosol pixels.

4.5. Feature importance analysis

Fig. 9 presents the global SHAP importance of the daytime and nighttime input variables. During daytime, the 12.02 μm brightness temperature made the largest contribution (10.6%), followed by the 3.75 μm brightness temperature (9.5%) and the 0.645-μm reflectance (8.5%). This ranking shows that the model jointly used thermal-emission and solar-reflective information. The combined importance of the 8.55, 11.03, and 12.02 μm channels is consistent with the emissivity contrasts of mineral dust across the 8 to 12 μm atmospheric window. The 3.75 μm channel provides complementary information because daytime radiances at this wavelength contain both reflected solar radiation and terrestrial thermal emission.

At night, thermal-infrared variables accounted for approximately 76.6% of the total contribution. The 12.02 μm brightness temperature was the most influential variable (12.0%), followed by the 13.34 μm brightness temperature (11.4%), skin temperature (11.0%), and the 8.55-μm brightness temperature (10.9%). The 12.02 and 8.55 μm channels characterize dust-related emissivity contrasts, whereas the 13.34 μm CO_2 absorption channel provides complementary sensitivity to high clouds. The contributions of skin temperature and land cover demonstrate the importance of the surface thermal background for reducing confusion among dust aerosol, cloud, and bare land. The contribution of the viewing zenith angle increased from 3.2% during daytime to 5.8% at night, suggesting greater sensitivity to atmospheric path length when solar-reflective observations were unavailable. Because SHAP values quantify model dependence rather than independent physical sensitivity, the contributions of correlated infrared channels should be interpreted jointly.

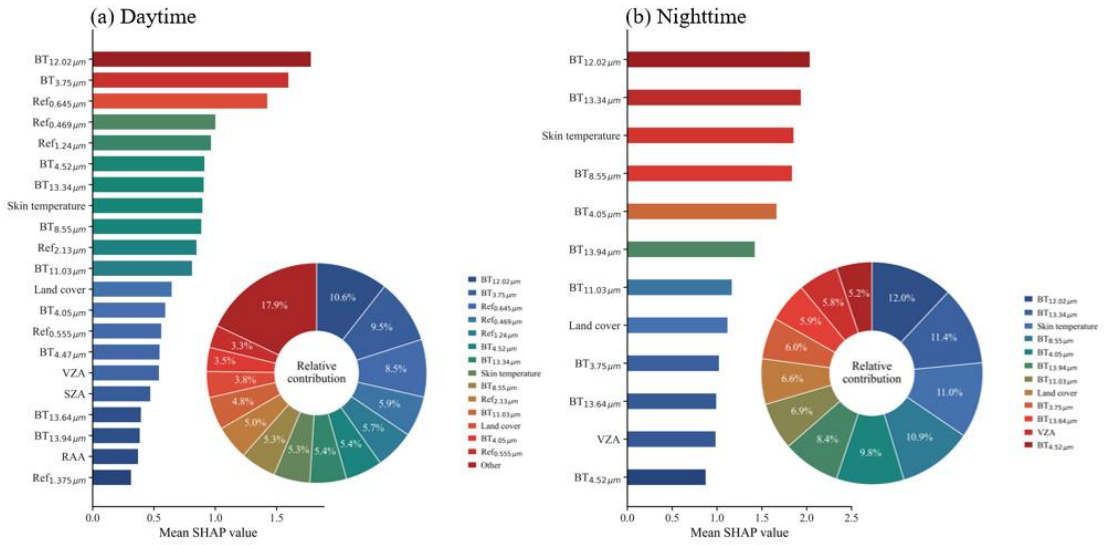


Fig. 9. SHAP-based feature importance and relative contributions for the (a) daytime and (b) nighttime SDE-Net models.

5. Conclusion

This study developed a physics-guided transfer-learning framework for cloud and dust aerosol identification over bright surfaces using MODIS multispectral observations. Radiative transfer simulations were used for pretraining, and collocated MODIS-CALIPSO observations were used for fine-tuning. The resulting SDE-Net discriminated among clear sky, cloud, and dust aerosol with overall accuracies of 93.81% during daytime and 85.68% at night.

Evaluation against multiple comparison methods demonstrated consistent improvements in both dust and cloud identification. The proposed method achieved an overall dust detection accuracy of 91.96%, with daytime and nighttime dust F1 scores of 87.80% and 77.04%, respectively. Cloud F1 scores reached 96.35% during daytime and 94.26% at night, exceeding those of both MYD35 configurations. The case studies further showed that the retrieved dust and cloud patterns were spatially coherent and consistent with MODIS imagery and CALIPSO vertical feature observations.

The stochastic formulation enabled separate evaluation of epistemic and aleatoric uncertainty. Mean epistemic uncertainty remained low at 1.71% during daytime and 5.69% at night, indicating that most test observations were represented by the learned model. Mean aleatoric uncertainty was

substantially higher and increased from 14.96% during daytime to 31.40% at night. This pattern indicates that the principal limitation is ambiguity in the available MODIS observations, particularly at night, when the absence of solar-reflective bands reduces the spectral separability of clouds, dust aerosol, and the underlying surface.

The results demonstrate the value of combining physically comprehensive simulations with sparse but vertically resolved lidar observations. Future work should improve the representativeness of reference labels by incorporating observations from ground-based lidar networks, refine the radiative transfer simulations using more detailed aerosol mixtures and surface properties, and evaluate transferability to other satellite sensors. Extension to geostationary platforms would also enable examination of the subdaily evolution of cloud and dust distributions.

Author contributions

S.W.: Writing – original draft, Writing – review & editing, Visualization, Methodology, Software, Validation, Formal analysis, Investigation, Data curation. T.W.: Supervision, Project administration, Resources, Funding acquisition, Writing – review & editing, Methodology. Y.J.: Data curation, Methodology, Validation. W.H.: Formal analysis. J.L.: Data curation, Methodology. X.M.: Writing – review & editing, Methodology. J.T.: Data curation, Investigation. F.Y.: Investigation. C.Z.: Data curation. B.E.N.: Writing – review & editing. M.O.A.: Writing – review & editing, Investigation.

Declaration of competing interest

The authors declare that they have no known competing financial interests or personal relationships that could have appeared to influence the work reported in this paper.

Acknowledgments

This work was supported by the National Natural Science Foundation of China (grant 42375136), the Youth Innovation Team of the China Meteorological Administration (CMA2024QN13), and the "Tianchi Talents" Introduction Plan (2024). The authors acknowledge NASA for providing the Aqua MODIS and CALIPSO data and acknowledge the European Centre for Medium-Range Weather Forecasts and the Copernicus Climate Change Service for providing the ERA5 reanalysis.

References

Ackerman, S.A., 1989. Using the radiative temperature difference at 3.7 and 11 μm to track dust outbreaks. Remote Sens. Environ. 27, 129–133.

Ackerman, S.A., 1997. Remote sensing aerosols using satellite infrared observations. J. Geophys. Res. 102, 17069–17079.

Ackerman, S.A., Strabala, K.I., Menzel, W.P., Frey, R.A., Moeller, C.C., Gumley, L.E., 1998. Discriminating clear sky from clouds with MODIS. J. Geophys. Res. Atmos. 103, 32141–32157.

Albarakat, R., Lakshmi, V., 2019. Monitoring dust storms in Iraq using satellite data. Sensors 19, 3687.

Anderson, G.P., Clough, S.A., Kneizys, F.X., Chetwynd, J.H., Shettle, E.P., 1986. AFGL atmospheric constituent profiles (0–120 km) (No. AFGL-TR-86-0110). Air Force Geophysics Laboratory, Hanscom AFB, MA, USA.

Arola, A., Lipponen, A., Kolmonen, P., Virtanen, T.H., Bellouin, N., Grosvenor, D.P., Gryspeerdt, E., Quaas, J., Kokkola, H., 2022. Aerosol effects on clouds are concealed by natural cloud heterogeneity and satellite retrieval errors. Nat. Commun. 13, 7357.

Aybar, C., Bautista›, L., Montero, D., Contreras, J., Ayala, D., Prudencio, F., et al., 2024. CloudSEN12+: The largest dataset of expert-labeled pixels for cloud and cloud shadow detection in Sentinel-2. Data Brief 56, 110852.

Baum, B.A., et al., 2011. Improvements in shortwave bulk scattering and absorption models for the remote sensing of ice clouds. J. Appl. Meteorol. Climatol. 50, 1037–1056.

Boloorani, A.D., Papi, R., Soleimani, M., Al-Hemoud, A., Amiri, F., Karami, L., et al., 2023. Visual interpretation of satellite imagery for hotspot dust sources identification. Remote Sens. Appl. Soc. Environ. 29, 100888.

Chen, Z., Torres, O., McCormick, M.P., Smith, W., Ahn, C., 2012. Comparative study of aerosol and cloud detected by CALIPSO and OMI. Atmos. Environ. 51, 187–195.

Derrien, M., Farki, B., Harang, L., LeGleau, H., Noyalet, A., Pochic, D., Sairouni, A., 1993. Automatic cloud detection applied to NOAA-11/AVHRR imagery. Remote Sens. Environ. 46, 246–267.

Di Biagio, C., Formenti, P., Balkanski, Y., Caponi, L., Cazaunau, M., Pangui, E., Journet, E., Nowak, S., Andreae, M.O., Kandler, K., Saeed, T., Piketh, S., Seibert, D., Williams, E., Doussin, J.-F., 2019. Complex refractive indices and single-scattering albedo of global dust aerosols in the shortwave spectrum and relationship to size and iron content. Atmos. Chem. Phys. 19, 15503–15531.

Emde, C., Buras-Schnell, R., Kylling, A., Mayer, B., Gasteiger, J., Hamann, U., Kylling, J., Richter, B., Pause, C., Dowling, T., Bugliaro, L., 2016. The libRadtran software package for radiative transfer calculations (version 2.0.1). Geosci. Model Dev. 9, 1647–1672.

Foga, S., Scaramuzza, P.L., Guo, S., Zhu, Z., Dilley Jr., R.D., Beckmann, T., et al., 2017. Cloud detection algorithm comparison and validation for operational Landsat data products. Remote Sens. Environ. 194, 379–390.

Fu, D., Shi, H., Gueymard, C.A., Yang, D., Zheng, Y., Che, H., et al., 2024. A deep-learning and transfer-learning hybrid aerosol retrieval algorithm for FY4-AGRI: Development and verification over Asia. Engineering 38, 164–174.

Fuell, K.K., Guyer, B.J., Kann, D., Molthan, A.L., Elmer, N., 2016. Next generation satellite RGB dust imagery leads to operational changes at NWS Albuquerque. J. Oper. Meteorol. 4, 62–78.

Gui, S., Song, S., Qin, R., Tang, Y., 2024. Remote sensing object detection in the deep learning era—a review. Remote Sens. 16, 327.

Gupta, R., Panchal, P., 2015. Advancement of cloud detection algorithm in satellite images with application to color models, in: 2015 International Conference on Computer Communication and Informatics (ICCCI). IEEE, pp. 1–6.

Hagihara, Y., Okamoto, H., Yoshida, R., 2010. Development of a combined CloudSat-CALIPSO cloud mask to show global cloud distribution. J. Geophys. Res. Atmos. 115, D4.

Hou, P., Guo, P., Wu, P., Wang, J., Gangopadhyay, A., Zhang, Z., 2020. A deep learning model for detecting dust in Earth's atmosphere from satellite remote sensing data, in: 2020 IEEE International Conference on Smart Computing (SMARTCOMP). IEEE, pp. 196–201.

Hsu, N.C., Jeong, M.J., Bettenhausen, C., Sayer, A.M., Hansell, R., Seftor, C.S., et al., 2013. Enhanced Deep Blue aerosol retrieval algorithm: The second generation. J. Geophys. Res. Atmos. 118, 9296–9315.

Jia, H., Ma, X., Yu, F., Quaas, J., 2021. Significant underestimation of radiative forcing by aerosol-cloud interactions derived from satellite-based methods. Nat. Commun. 12, 3649.

Jiao, Y., Zhang, M., Wang, L., Qin, W., 2023. A new cloud and haze mask algorithm from radiative transfer simulations coupled with machine learning. IEEE Trans. Geosci. Remote Sens. 61, 1–16.

Jiao, Y., Wang, T., Wang, S., Si, Y., Chen, L., Zheng, Y., Yang, F., Zhou, C., Yang, L., Nishonov, B.E., Amonov, M.O., 2026. A novel physics-informed transformer algorithm (PITA) for near-real-time synergistic multiparameter aerosol retrieval from FY-4B/AGRI geostationary satellite. IEEE Trans. Geosci. Remote Sens. 64, 4108324.

Jin, J., Zhang, F., Li, W., Wu, Q., Mei, L., Chen, L., 2023. A hybrid algorithm for dust aerosol detection: Integrating forward radiative transfer simulations and machine learning. IEEE Trans. Geosci. Remote Sens. 61, 1–15.

Karimi, N., Moridnejad, A., Golian, S., Samani, J.M.V., Karimi, D., Javadi, S., 2012. Comparison of dust source identification techniques over land in the Middle East region using MODIS data. Can. J. Remote Sens. 38, 586–599.

Kazi, A.K., Nagatani, I., Kawano, K., Kudoh, J.-I., 2019. Development of a new dust index NDLI for Asian dust extraction system based on Aqua MODIS data and monitoring of trans-boundary Asian dust events in Japan. Int. J. Remote Sens. 40, 1030–1047.

Kim, D., Chin, M., Yu, H., Eck, T.F., Sinyuk, A., Smirnov, A., Holben, B.N., 2011. Dust optical properties over North Africa and Arabian Peninsula derived from the AERONET dataset. Atmos. Chem. Phys. 11, 10733–10741.

Kindel, B.C., Pilewskie, P., Schmidt, K.S., Coddington, O., King, M.D., 2011. Solar spectral absorption by marine stratus clouds: Measurements and modeling. J. Geophys. Res. 116, D10203.

King, M.D., Tsay, S.-C., Platnick, S.E., Wang, M., Liou, K.N., 1997. Cloud retrieval algorithms for MODIS: Optical thickness, effective particle radius, and thermodynamic phase. NASA Goddard Space Flight Center, MODIS Algorithm Theoretical Basis Document.

Kokhanovsky, A.A., Breon, F.M., Cacciari, A., Carboni, E., Diner, D., Di Nicolantonio, W., et al., 2007. Aerosol remote sensing over land: A comparison of satellite retrievals using different algorithms and instruments. Atmos. Res. 85, 372–394.

Kong, L., Sun, J., Zhang, C., 2020. SDE-Net: Equipping deep neural networks with uncertainty estimates, in: Proceedings of the 37th International Conference on Machine Learning (ICML), Proceedings of Machine Learning Research. JMLR.org, pp. 5405–5415.

Kussul, N., Lavreniuk, M., Skakun, S., Shelestov, A., 2017. Deep learning classification of land cover and crop types using remote sensing data. IEEE Geosci. Remote Sens. Lett. 14, 778–782.

Le Borgne, P., Péré, S., Roquet, H., 2013. Night time detection of Saharan dust using infrared window channels: Application to NPP/VIIRS. Remote Sens. Environ. 137, 264–273.

Lee, J., Shi, Y.R., Cai, C., Ciren, P., Wang, J., Gangopadhyay, A., Zhang, Z., 2021. Machine learning based algorithms for global dust aerosol detection from satellite images: Inter-comparisons and evaluation. Remote Sens. 13, 456.

Li, J., Menzel, W.P., Yang, Z., Frey, R.A., Ackerman, S.A., 2003. High-spatial-resolution surface and cloud-type classification from MODIS multispectral band measurements. J. Appl. Meteorol. 42, 204–226.

Li, X., Song, W., 2009. Dust storm detection based on MODIS data, in: Proceedings of the International Conference on Geo-spatial Solutions for Emergency Management and the 50th Anniversary of the Chinese Academy of Surveying and Mapping, Beijing, China, pp. 14–19.

Loveland, T.R., Belward, A.S., 1997. The IGBP-DIS global 1 km land cover data set, DISCover: First results. Int. J. Remote Sens. 18, 3289–3295. https://doi.org/10.1080/014311697217099.

Mahajan, S., Fataniya, B., 2020. Cloud detection methodologies: Variants and development—a review. Complex Intell. Syst. 6, 251–261.

Mishchenko, M.I., Travis, L.D., Lacis, A.A., 2002. Scattering, Absorption, and Emission of Light by Small Particles. Cambridge University Press, Cambridge.

Nakajima, T.Y., Tsuchiya, T., Ishida, H., Matsui, T.N., Shimoda, H., 2011. Cloud detection performance of spaceborne visible-to-infrared multispectral imagers. Appl. Opt. 50, 2601–2616.

Pan, S.J., Yang, Q., 2009. A survey on transfer learning. IEEE Trans. Knowl. Data Eng. 22, 1345–1359.

Park, S.S., Kim, J., Lee, J., Lee, S., Kim, J.S., Chang, L.S., Ou, S., 2014. Combined dust detection algorithm by using MODIS infrared channels over East Asia. Remote Sens. Environ. 141, 24–39.

Platnick, S., King, M.D., Ackerman, S.A., Menzel, W.P., Baum, B.A., Riédi, J.C., Frey, R.A., 2003. The MODIS cloud products: Algorithms and examples from Terra. IEEE Trans. Geosci. Remote Sens. 41, 459–473.

Platnick, S., Meyer, K.G., King, M.D., Wind, G., Amarasinghe, N., Marchant, B., Arnold, G.T., Zhang, Z., Hubanks, P.A., Holz, R.E., Yang, P., Ridgway, W.L., Riédi, J., 2017. The MODIS cloud optical and microphysical products: Collection 6 updates and examples from Terra and Aqua. IEEE Trans. Geosci. Remote Sens. 55, 502–525.

Qu, J.J., Hao, X., Kafatos, M., Wang, L., 2006. Asian dust storm monitoring combining Terra and Aqua MODIS SRB measurements. IEEE Geosci. Remote Sens. Lett. 3, 484–486.

Rasmussen, C.B., Kirk, K., Moeslund, T.B., 2022. The challenge of data annotation in deep learning—a case study on whole plant corn silage. Sensors 22, 1596.

Rivas-Perea, P., Rosiles, J.G., Cota-Ruiz, J., 2013. Statistical and neural pattern recognition methods for dust aerosol detection. Int. J. Remote Sens. 34, 7648–7670. https://doi.org/10.1080/01431161.2013.822660.

Roskovensky, J., Liou, K., 2003. Detection of thin cirrus from 1.38 μm/0.65 μm reflectance ratio combined with 8.6–11 μm brightness temperature difference. Geophys. Res. Lett. 30. https://doi.org/10.1029/2003GL018135.

Roskovensky, J., Liou, K., 2005. Differentiating airborne dust from cirrus clouds using MODIS data. Geophys. Res. Lett. 32. https://doi.org/10.1029/2005GL022798.

Shi, L., Zhang, J., Zhang, D., Igbawua, T., Liu, Y., 2020. Developing a dust storm detection method combining support vector machine and satellite data in typical dust regions of Asia. Adv. Space Res. 65, 1263 – 1278. https://doi.org/10.1016/j.asr.2019.11.027.

Souri, A.H., Vajedian, S., 2015. c J. Earth Syst. Sci. 124, 1127–1141. https://doi.org/10.1007/s12040-015-0585-6.

Stamnes, K., et al., 2018. Progress in forward-inverse modeling based on radiative transfer tools for coupled atmosphere-snow/ice-ocean systems: A review and description of the AccuRT model. Appl. Sci. 8, 2682. https://doi.org/10.3390/app8122682.

Tang, C., Shi, C., Letu, H., Yin, S., Nakajima, T., Sekiguchi, M., et al., 2025. Development of a hybrid algorithm for the simultaneous retrieval of aerosol optical thickness and fine-mode fraction from multispectral satellite observation combining radiative transfer and transfer learning approaches. Remote Sens. Environ. 319, 114619.

Torrey, L., Shavlik, J., 2010. Transfer learning, in: Handbook of Research on Machine Learning Applications and Trends: Algorithms, Methods, and Techniques. IGI Global Scientific Publishing, pp. 242–264.

Vaswani, A., Shazeer, N., Parmar, N., Uszkoreit, J., Jones, L., Gomez, A.N., Kaiser, L., Polosukhin, I., 2017. Attention is all you need. Advances in Neural Information Processing Systems 30.

Wald, A.E., Kaufman, Y.J., Tanré, D., Gao, B.C., 1998. Daytime and nighttime detection of mineral dust over desert using infrared spectral contrast. J. Geophys. Res. 103, 32307–32313.

Wang, S., Wang, T., Jiao, Y., Dong, Y., Li, J., Bi, J., Huo, Y., Amonov, M.O., Abdullaev, S., 2024. Global aerosol models considering their spatial heterogeneities based on AERONET measurements. Atmos. Res. 308, 107521.

Wang, Z., Zhang, J., Bai, L., Chang, H., Chen, Y., Zhang, Y., Tao, J., 2024. A deep learning based platform for remote sensing images change detection integrating crowdsourcing and active learning. Sensors 24, 1509.

Weiss, K., Khoshgoftaar, T.M., Wang, D., 2016. A survey of transfer learning. J. Big Data 3, 9.

Wu, Z., Li, J., Wang, Y., Hu, Z., Molinier, M., 2019. Self-attentive generative adversarial network for cloud detection in high resolution remote sensing images. IEEE Geosci. Remote Sens. Lett. 17, 1792–1796.

Xu, M., Deng, F., Jia, S., Jia, X., Plaza, A.J., 2022. Attention mechanism-based generative adversarial networks for cloud removal in Landsat images. Remote Sens. Environ. 271, 112902.

Yue, H., He, C., Zhao, Y., Ma, Q., Zhang, Q., 2017. The brightness temperature adjusted dust index: An improved approach to detect dust storms using MODIS imagery. Int. J. Appl. Earth Obs. Geoinf. 57, 166–176.

Zhang, B., Zhang, Y., Li, Y., Wan, Y., Yao, Y., 2022. CloudViT: A lightweight vision transformer network for remote sensing cloud detection. IEEE Geosci. Remote Sens. Lett. 20, 1–5.

Zhang, L., Zhang, L., Du, B., 2016. Deep learning for remote sensing data: A technical tutorial on the state of the art. IEEE Geosci. Remote Sens. Mag. 4, 22–40.

Zhang, X., Wang, H., Che, H.Z., Tan, S.C., Shi, G.Y., Yao, X.P., 2020. The impact of aerosol on MODIS cloud detection and property retrieval in seriously polluted East China. Sci. Total Environ. 711, 134634.

Zhen, Z., Li, Z., Wang, F., Xu, F., Li, G., Zhao, H., et al., 2024. CNN-LSTM networks based sand and dust storms monitoring model using FY-4A satellite data. IEEE Trans. Ind. Appl. 60, 5130–5141.

Zhu, X.X., Tuia, D., Mou, L., Xia, G.S., Zhang, L., Xu, F., Fraundorfer, F., 2017. Deep learning in remote sensing: A comprehensive review and list of resources. IEEE Geosci. Remote Sens. Mag. 5, 8–36.

Zhuang, F., Qi, Z., Duan, K., Xi, D., Zhu, Y., Zhu, H., et al., 2020. A comprehensive survey on transfer learning. Proc. IEEE 109, 43–76.

Supplementary Files

This is a list of supplementary files associated with this preprint. Click to download.

- SupplementaryMaterial.docx